ChemPubSoc Europe

DOI: 10.1002/chem.201902339

CHEMISTRY A European Journal Full Paper

Coordination Chemistry |*Hot Paper*|

Coordination Chemistry of P_4S_3 and P_4Se_3 towards the Iron Fragments $[Fe(Cp)(CO)_2]^+$ and $[Fe(Cp)(PPh_3)(CO)]^+$

Philippe Weis,[a] Ian M. Riddlestone,[b] Harald Scherer,[a] and Ingo Krossing*[a]

Abstract: The complexes $Ag(L)_n[WCA]$ (L = P_4S_3, P_4Se_3, As_4S_3, and As_4S_4; [WCA] = $[Al(OR^F)_4]^-$ and $[F\{Al(OR^F)_3\}_2]^-$; R^F = $C(CF_3)_3$; WCA = weakly coordinating anion) were tested for their performance as ligand-transfer reagents to transfer the poorly soluble nortricyclane cages P_4S_3, P_4Se_3, and As_4S_3 as well as realgar As_4S_4 to different transition-metal fragments. As_4S_4 and As_4S_3 with the poorest solubility did not yield complexes. However, the more soluble silver-coordinated P_4S_3 and P_4Se_3 cages were transferred to the electron-poor Fp^+ moiety ($[CpFe(CO)_2]^+$). Thus, reaction of the silver salt in the presence of the ligand with *Fp*–Br yielded [*Fp*–P_4S_3] $[Al(OR^F)_4]$ (**1 a**), [*Fp*–P_4S_3][$F(Al(OR^F)_3)_2$] (**1 b**), and [*Fp*–P_4Se_3] $[Al(OR^F)_4]$ (**2**). Reactions with P_4S_3 also yielded [*Fp*PPh_3–P_4S_3] $[Al(OR^F)_4]$ (**3**), a complex with the more electron-rich monophosphine-substituted Fp^+ analogue $[FpPPh_3]^+$ ($[CpFe(PPh_3)(CO)]^+$). All complex salts were characterized by single-crystal XRD, NMR, Raman, and IR spectroscopy. Interestingly, they show characteristic blueshifts of the vibrational modes of the cage, as well as structural contractions of the cages upon coordination to the *Fp*/*Fp*PPh_3 moieties, which oppose the typically observed cage expansions that lead to redshifts in the spectra. Structure, bonding, and thermodynamics were investigated by DFT calculations, which support the observed cage contractions. Its reason is assigned to σ and π donation from the slightly P–P and P–E antibonding P_4E_3-cage HOMO (*e* symmetry) to the metal acceptor fragment.

Introduction

Next to the known examples of neutral complexes of P_4E_3 (E = S, Se) cages with BX_3 (X = Br, I), $NbCl_5$, Ni(np3) (np3 = tris(2-(diphenylphosphino)ethyl)amine), $M(CO)_5$ (M = Mo, W), $CuX(PR_3)_2$ (X = Cl, Br, I; R = Me, Et, *i*Pr, Cy), and $Cp^*V(CO)_3$,[1] cationic complexes that use these cages as ligands include electron-rich transition-metal fragments, mostly 16 valence electron iron or ruthenium. The presence of electron-rich phosphines or additionally the pentamethylcyclopentadienide (Cp*) ligand is hitherto paramount for stability; typical examples include $[Fe(Cp)(dppe)(P_4S_3)]^+$ and $[Ru(Cp^*)(dppe)P_4Se_3]^+$ (dppe = bis(diphenylphosphino)ethane) (Figure 1). In such complexes, the basal phosphorus atoms of the cage coordinate to the metal atom, or as in dimeric $[\{Ru(Cp)(PPh_3)_2\}_2P_4S_3]^{2+}$, the nortricyclane cage interacts with the metal fragments through the apical as well as one of the basal phosphorus atoms.[2,3–5] Complexes of these transition-metal fragments with other inorganic cages as ligands, such as P_4, As_4, and AsP_3, also exist; for example, $[Cp^*Fe(dppe)(P_3As)]^+$, $[Cp^*Fe(dppe)(P_4)]^+$, and $[Cp^*Ru(dppe)(As_4)]^+$.[6,7] These complexes can enable interesting degradation chemistry of the otherwise inert cages under standard conditions. The hydrolysis of $[\{CpRu(PPh_3)_3\}_2(P_4)]^{2+}$ and $[\{CpRu(PPh_3)_3\}_2(P_4S_3)]^{2+}$ salts, for example, yield complexes of diphosphane and thiophosphinic acid.[5]

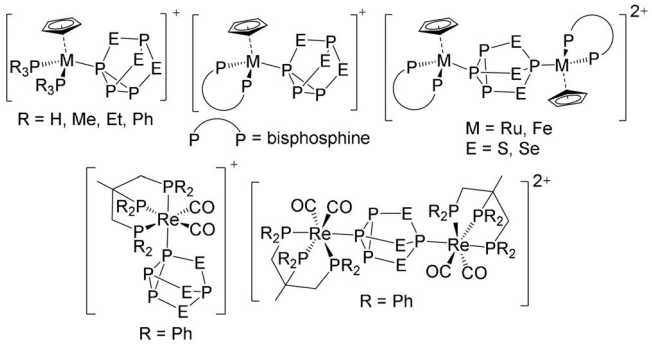

Figure 1. Examples of metal fragments known to form cationic complexes with the P_4E_3 cages.

A novel approach towards complexes of weak ligands, like the group 15/16 cages, are ligand-transfer reactions. Thus, Scheer et al. succeeded in the synthesis of complexes of yellow arsenic ($[PPh_3Au(As_4)]^+$ and $[Cp^*Ru(dppe)(As_4)]^+$) through the

[a] *P. Weis, Dr. H. Scherer, Prof. Dr. I. Krossing*
Institut für Anorganische und Analytische Chemie and
Freiburger Materialforschungszentrum (FMF), Universität Freiburg
Albertstr. 21, 79104 Freiburg (Germany)
E-mail: krossing@uni-freiburg.de

[b] *Dr. I. M. Riddlestone*
Department of Chemistry, University of Surrey
Guildford, GU2 7XH, Surrey (UK)

Supporting information and the ORCID identification number(s) for the author(s) of this article can be found under: https://doi.org/10.1002/chem.201902339.

reaction of the corresponding transition-metal halide with $Ag(As_4)_2[Al(OR^F)_4]$. This acts as a stable storage form of yellow arsenic that releases the As_4 cluster upon removal of the Ag^+ cation with a well-soluble halide complex.[7,8]

In this realm, the more electron-poor complex $[CpFe(CO)_2]^+$ (*Fp*$^+$) and monophosphine-substituted complex $[CpFe(CO)(PPh_3)]^+$ (*Fp*PPh_3^+) units are not known for coordination chemistry that uses such weak ligands. However, they readily yield complexes with strongly coordinating ligands, such as phosphines.[9] Only recently, [*Fp*–P_4]$^+$ and monophosphine-substituted [*Fp*PPh_3–P_4]$^+$ that include dynamically bound P_4 cages, which are visible on the NMR timescale, were synthesized.[10] The formation of these complexes showed that it is possible to use the ligand-transfer reaction to bind weak ligands to these metal fragments through halide abstractions given that the ligand is immediately present in the reaction environment by coordination to the silver ion. With this precaution, the reactivity of the metal fragment is not quenched by competing reactions, such as the formation of the adduct [*Fp*–Br–*Fp*]$^+$ with residual *Fp*–Br or the dismutation product $[CpFe(CO)_2PPh_3]^+$. Interestingly, characteristic blueshifts of the breathing modes of the P_4 ligand accompanied by a considerable shrinkage of the P–P bond lengths were observed in these complexes. Thus, apparently, the relatively electron-poor fragments *Fp*$^+$ and *Fp*PPh_3^+ induced a novel bonding situation of the P_4 ligand: The carbonyl-substituted metal fragments prevent π back-bonding, and the Fe–P interaction is reduced mainly to π donation from the P_4 cluster to the metal. As the HOMO of P_4 has some antibonding character, this results in a structural contraction of the cages. By contrast, the known examples with the more electron-rich metal fragments, such as $[CpFe(dppe)]^+$, form stable and NMR-static complexes with those ligands owing to a considerable amount of π back-bonding that cancels out this cage contraction.[10]

Yet, quite a number of complexes of weak and often poorly soluble ligands with the silver ion of $Ag[Al(OR^F)_4]$ are accessible; that is, those with inorganic rings, such as S_8, Se_n ($n=6$, 12), and the cages P_4, P_4S_3, P_4Se_3, As_4S_3, and As_4S_4.[11,12–14] Hence, the concept of ligand-transfer chemistry can be tested by reacting easily accessible representatives of these compounds with suitable, soluble transition-metal halides. Herein, we present complexes of P_4S_3 and P_4Se_3 with the electron-poor iron fragments *Fp*$^+$ and *Fp*PPh_3^+. They are the first examples of such complexes that do not rely on bidentate phosphine and the electron-rich Cp* ligands. These complexes show similar blueshifts of their vibrational modes and cage contractions upon coordination to the metal, as in [*Fp*–P_4]$^+$ and [*Fp*PPh_4–P_4]$^+$.

Results and Discussion

Synthesis of the complexes

Generally, the synthesis of the complexes was achieved by weighing one equivalent of Ag[WCA] (WCA = weakly coordinating anion) together with one equivalent of the ligand on one side of a double-bulb vessel that was separated by a glass frit plate and condensing CH_2Cl_2 onto the solids. After stirring for 1 h at room temperature, the solids were dissolved, and a solution of one equivalent of [M]X (X = *Fp*–Br, *Fp*PPh_3–Br, or PPh_3AuCl) in CH_2Cl_2 was added to the reaction mixture (Scheme 1). Immediately, a precipitate of AgBr formed and a

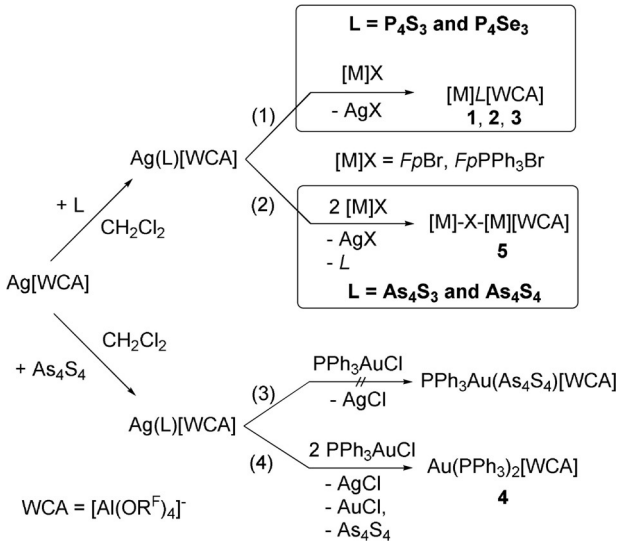

Scheme 1. Schematic overview of the formation of $[ML]^+$ complexes from silver complexes of weak ligands.

color change of the yellow-orange solution to deep red occurred (not for PPh_3AuCl). After stirring for several hours to ensure a complete reaction and removal of AgBr by filtration, the obtained deep red solutions were reduced in volume to around half and layered with pentane. Storage of these mixtures at room temperature or at 6 °C led to the formation of crystals after several days. For P_4S_3 and P_4Se_3, this procedure led to complexes **1**, **2**, and **3** (Scheme 1, Reaction 1). The synthesis of complex **1** was done with the $[Al(OR^F)_4]^-$ (**1a**) as well as the $[F(Al(OR^F)_3)_2]^-$ anion (**1b**) to tackle problems with the structural characterization. Syntheses of the potential $[Fp(As_4S_4)]^+$, $[Fp(As_4S_3)]^+$, and $[(PPh_3)Au(As_4S_4)]^+$ complex salts were futile with all conditions tested (Scheme 1, Reactions 2–4); instead, the reactions led to a precipitate of free ligand and crystals of $Au(PPh_3)_2[Al(OR^F)_4]$ (**4**) or *Fp*–Br–*Fp*$[Al(OR^F)_4]$ (**5**). The cations [*Fp*–Br–*Fp*]$^+$ as well as $[Au(PPh_3)_2]^+$ are already known.[15]

NMR spectra of the complexes

The NMR spectra of isolated crystals of complexes **1a**, **2**, and **3** dissolved in CD_2Cl_2 show that the used $[Al(OR^F)_4]^-$ anion stays intact over the course of the reactions because only the typical ^{19}F and ^{27}Al NMR signals are visible (see the Supporting Information, Figures S4–S24). Owing to their dynamic nature in solution, the known silver complexes $Ag(P_4S_3)_n[WCA]$[12,13] and $Ag(P_4Se_3)_n[WCA]$ ($n=1$, 2 3)[14] show only two distinct signals of the ligands in the ^{31}P NMR spectra. Complexes **1** and **2** show three distinct signals of the apical phosphorus atom P_a, the coordinated basal phosphorus atom $P_{b/coord}$, and the noncoordi-

nated phosphorus atoms $P_{b/noncoord}$. This demonstrates that the P_4Se_3 and P_4S_3 cages are firmly bound to the *Fp* moiety through one of their basal phosphorus atoms, similar to the more electron-rich analogues $[Cp^*Ru(L_2)(P_4S_3)]^+$ and $[Cp^*Ru(L_2)(P_4Se_3)]^+$ (L_2 = bidentate phosphine) but unlike the more weakly bound P_4 ligand in $[Fp{-}P_4]^+$.[3,10] Complex **3** shows five different phosphorus signals, one for the PPh_3 ligand and four for the P_4S_3 cage. An apical coordination of the cages would exhibit less cage signals, as known from studies of ruthenium 16 electron fragments coordinated to P_4S_3 that include a mixture of isomers. Isomer formation did not occur for P_4Se_3.[3] However, apical coordination of P_4S_3 was observed to a low extent in complexes **1** (<1%) and **3** (5%). All ^{31}P NMR spectra are summarized in Figure 2.

All ^{31}P chemical shifts as well as the coupling constants are given in Table 1. Complexes **1** and **2** exhibit an ABX_2 spin system with slightly higher order effects in their $^{31}P\{^1H\}$ NMR spectra. In the non-decoupled ^{31}P spectra, $P_{b/coord}$ shows further splitting, which is due to the coupling of the five protons of the Cp ring to $P_{b/coord}$ with $^3J(^1H, ^{31}P_{b/coord}) = 2$ Hz in both cases. The resonance of the apical phosphorus atoms P_a in complexes **1** and **2** manifests as a triplet of doublets. The signals of the coordinated basal phosphorus atoms $P_{b/coord}$ show a signal that resembles a triplet of doublets, but it includes further splitting of the central line of the triplet owing to slightly higher order effects. The noncoordinated basal phosphorus atoms $P_{b/noncoord}$ also show a signal that resembles a doublet of doublets, but this shows further splitting owing to slightly higher order effects.

Owing to the loss of the chemical equivalency of the two $P_{b/noncoord}$ atoms in complex **3**, the $^{31}P\{^1H\}$ NMR spectra of this compound show an ABFMX spin system with dddd splittings for each phosphorus atom, with the coupling constants $^1J(P_{b/coord}, P_{b/noncoord1}) = 236$, $^1J(P_{b/coord}, P_{b/noncoord2}) = 233$, $^2J(P_a, P_{b/noncoord1}) = 75$, $^2J(P_a, P_{b/noncoord2}) = 73$, $^1J(P_{b/noncoord1}, P_{b/noncoord2}) = 56$, $^2J(P_{b/coord}, P_{PPh_3}) = 44$, $^2J(P_a, P_{b/coord}) = 47$, $^3J(P_{b/noncoord1}, P_{PPh_3}) = 4$, and $^3J(P_{b/noncoord2}, P_{PPh_3}) = 1$ Hz, as well as the $^5J(P_a, P_{PPh_3})$ coupling, which is below 1 Hz. The two $P_{b/noncoord}$ atoms are not chemically equivalent in complex **3**; therefore, the two atoms $P_{b/noncoord1}$ and $P_{b/noncoord2}$ can be found at two different chemical shifts of −133.6 and −139.2 ppm, respectively. Again, further splittings of the signals are notable in the non-decoupled ^{31}P spectra, because the protons of the Cp ligand couple to the phosphorus atoms in the P_4S_3 cage.

The coordination of Fp^+ and $FpPPh_3^+$ moieties to the P_4S_3 and P_4Se_3 cages significantly alters their chemical shifts: The apical phosphorus atoms P_a are shifted slightly downfield upon coordination of one of the basal phosphorus atoms to the metal. The noncoordinated basal phosphorus atoms $P_{b/noncoord}$ are only moderately shielded with respect to P_b of free P_4S_3 and P_4Se_3 (shifted upfield, $\delta = 7$ to 10.5 ppm). The coordinated basal phosphorus atoms $P_{b/coord}$ experience a strong downfield shift to $\delta = 139.3$ (**1a**), 157.8 (**2**), and 126.6 ppm (**3**). It is notable that this shift is larger in the phosphine-substituted example. This is consistent with other complexes of P_4S_3 and P_4Se_3 with the metal fragments $[(Cp^*)Ru(L')]^+$ (L′ = dppe, dppm, dppet, dpadppe) that have shown similar trends of the chemical shifts. The shift of $P_{b/coord}$ is stronger in the examples with bisphosphine ligands. In contrast to complexes **1**, **2**, and **3**, which are firmly bound at room temperature, the recently synthesized complex $[Fp{-}P_4]^+[Al(OR^F)_4]^-$ shows fluctuating behavior at room temperature that can be frozen out at temperatures below 263 K.[10]

The ^{77}Se spectra (see the Supporting Information, Figure S16) of complex **2** shows that the multiplet of the P_4Se_3 cages in $Ag(P_4Se_3)_n[Al(OR^F)_4]$, which can be found at $\delta \approx 800$ ppm,[14] splits into two distinct signals at $\delta = 775$ and 622 ppm, with the high-field shifted signal at $\delta = 622$ ppm

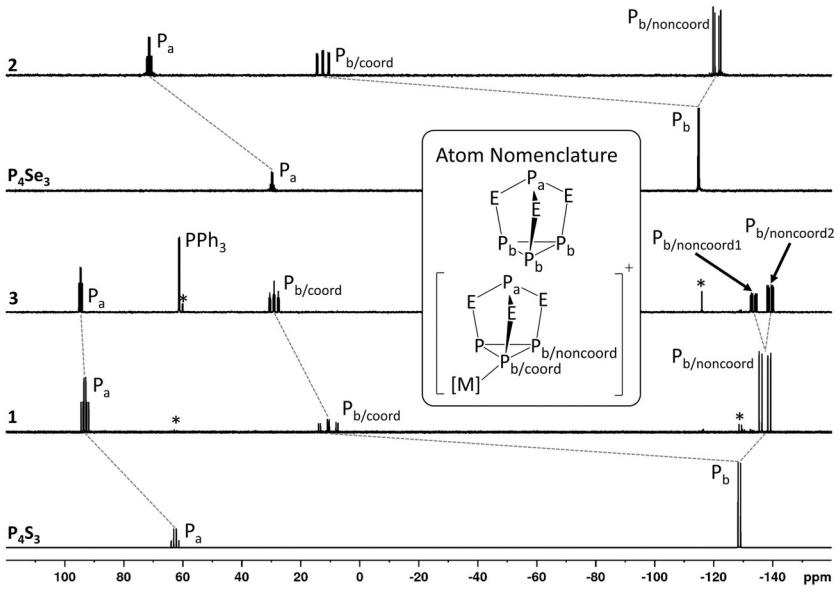

Figure 2. ^{31}P NMR spectra of complexes **1**, **2**, and **3** as well as the free ligands P_4S_3 and P_4Se_3 in CD_2Cl_2 at room temperature. Close-up views of the splitting patterns are given in the Supporting Information. The asterisk (*) denotes minor amounts of noncoordinated P_4S_3 (in the spectrum of complex **1**) and/or apically coordinated P_4S_3 (in the spectrum of complex **3**). The stippled lines indicate the changes of the chemical shifts and splittings of the signals upon coordination of the ligand.

Table 1. ^{31}P chemical shifts as well as coupling constants and multiplicities of the signals of complexes **1a**, **2**, and **3** alongside free ligands P_4S_3 and P_4Se_3 in CD_2Cl_2 at room temperature.[a]

	Spin system	P_a	$P_{b/coord}$	$P_{b/noncoord}$	PPh_3
P_4S_3	AB_3	62.6 ppm (q) $^2J(P_b, P_a) = 71$ Hz	−128.7 ppm (d) $^2J(P_b, P_a) = 71$ Hz	–	–
1a	ABX_2[b]	93.2 ppm (td) $^2J(P_a, P_{b/noncoord}) = 79$ Hz $^2J(P_a, P_{b/coord}) = 51$ Hz	10.6 ppm (m[b]) $^1J(P_{b/coord}, P_{b/noncoord}) = 239$ Hz $^2J(P_a, P_{b/coord}) = 51$ Hz	−137.4 ppm (m[b]) $^1J(P_{b/coord}, P_{b/noncoord}) = 239$ Hz $^2J(P_a, P_{b/noncoord}) = 79$ Hz	–
3	ABFMX	94.7 ppm (dddd) $^2J(P_a, P_{b/noncoord1}) = 75$ Hz $^2J(P_a, P_{b/noncoord2}) = 73$ Hz $^2J(P_a, P_{b/coord}) = 47$ Hz $^5J(P_a, P_{PPh_3}) = < 1$ Hz	29.1 ppm (dddd) $^1J(P_{b/coord}, P_{b/noncoord1}) = 236$ Hz $^1J(P_{b/coord}, P_{b/noncoord2}) = 233$ Hz $^2J(P_a, P_{b/coord}) = 47$ Hz $^2J(P_{PPh_3}, P_{b/coord}) = 44$ Hz	−133.6 ppm (dddd) (=$P_{b/noncoord1}$) $^1J(P_{b/coord}, P_{b/noncoord1}) = 236$ Hz $^2J(P_a, P_{b/noncoord1}) = 75$ Hz $^1J(P_{b/noncoord1}, P_{b/noncoord2}) = 56$ Hz $^3J(P_{b/noncoord1}, P_{PPh_3}) = 4$ Hz −139.2 ppm (dddd) (=$P_{b/noncoord2}$) $^1J(P_{b/coord}, P_{b/noncoord2}) = 233$ Hz $^2J(P_a, P_{b/noncoord2}) = 73$ Hz $^1J(P_{b/noncoord}, P_{b/noncoord2}) = 56$ Hz $^3J(P_{b/noncoord2}, P_{PPh_3}) = 1$ Hz	61.3 ppm (dddd) $^2J(P_{b/coord}, P_{PPh_3}) = 44$ Hz $^3J(P_{b/noncoord1}, P_{PPh_3}) = 4$ Hz $^3J(P_{b/noncoord2}, P_{PPh_3}) = 1$ Hz $^5J(P_a, P_{PPh_3}) = < 1$ Hz
P_4Se_3	AB_3	30.5 ppm (q) $^2J(P_b, P_a) = 72$ Hz	−114.1 ppm (d) $^2J(P_b, P_a) = 72$ Hz	–	–
2	ABX_2[b]	71.4 ppm (td) $^2J(P_a, P_{b/noncoord}) = 77$ Hz $^2J(P_a, P_{b/coord}) = 56$ Hz	12.5 ppm (m[b]) $^1J(P_{b/coord}, P_{b/noncoord}) = 240$ Hz $^2J(P_a, P_{b/coord}) = 56$ Hz	−121.1 ppm (m[b]) $^1J(P_{b/coord}, P_{b/noncoord}) = 240$ Hz $^2J(P_a, P_{b/noncoord}) = 77$ Hz	–

[a] All values of chemical shifts are given in ppm. Couplings to the protons are omitted in this list (see the Supporting Information). In the case of complex **3**, the coupling constants in the higher order spin systems are given in the Supporting Information (Table S3). [b] These spin systems show additional splittings owing to higher-order effects. Hence, the affected signals are marked as multiplets (m).

being caused by the single selenium atom next to $P_{b/coord}$. This signal shows a ddt splitting with the coupling constants ^1J(Se, $P_{b/coord}$) = 463, ^1J(Se, P_a) = 273, and ^2J(Se, $P_{b/noncoord}$) = 20 Hz). The resonance at $\delta = 775$ ppm is caused by the isotopomer that has one ^{77}Se atom in a position between P_a and $P_{b/noncoord}$ and shows a multiplet of higher order (see the Supporting Information, Table S3 for coupling constants). It should be noted that the coupling constant between the two $P_{b/noncoord}$ is exceptionally small for a ^1J(P, P) coupling. ^{77}Se NMR spectra of previously characterized similar compounds, such as [(Cp*)Ru(dppe)P_4Se_3][BPh_4] and other analogues were not reported owing to the limited solubility of the compounds.[3]

The ^{13}C NMR spectra of complexes **1a**, **2**, and **3** show signals for the Cp ligands at around $\delta = 88$ ppm. The CO ligands of complexes **2** and **3** are visible at $\delta = 205.4$ and 213.1 ppm, respectively, which is consistent with the data recorded for [*Fp*–P_4][WCA] and [*Fp*PPh_3–P_4][WCA].[10] ^{13}C NMR signals of the CO ligands in complex **1a** could not be obtained within a reasonable timeframe, and thus, are not given (but IR and Raman spectroscopy data are available).

Single-crystal structures

The crystals of compounds **1** to **3** were obtained as yellow to red blocks. We were not able to obtain a data set of complex **1a** because the crystals crack in the cooling stream of the diffractometer. Thus, complex **1b** was synthesized, which contains the same cation.[16] The crystal structures of complexes **4** and **5** were also determined and deposited[19] (see the Supporting Information, Table S1), but they are not discussed because they contain known cations. The asymmetric unit of all structures only contains one cation. All cations show the *Fp* or *Fp*PPh_3 moieties bound to one of the basal phosphorus atoms of the nortricyclane cage, which supports the findings from the NMR spectroscopy. The molecular structures of all cations are shown in Figure 3.

A summary of all relevant bond lengths is given in Table 2. All nortricyclane cages show slight contractions of the $P_{b/coord}$–$P_{b/noncoord}$ bonds of up to 4.1 pm in complex **3** compared with

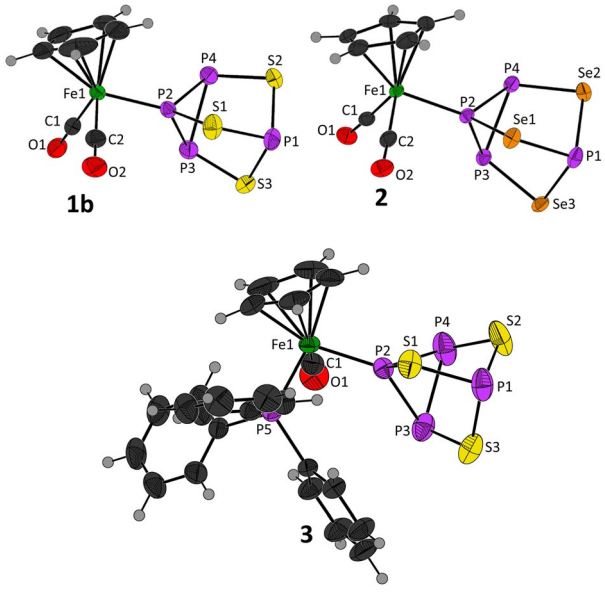

Figure 3. Molecular structures of complexes **1b** (100 K), **2** (100 K), and **3** (170 K). All thermal ellipsoids are shown at 50% probability. The anions have been omitted for reasons of clarity.

Table 2. Comparison of the structural parameters of complexes **1 b** (100 K), **2** (100 K), and **3** (170 K) with the free ligands P_4S_3 and P_4Se_3 at 100 K. E denotes the chalcogen atoms of the ligand (S or Se). Calculated bond distances with index "calc." are given ((RIJ)B3-LYP(D3BJ)/def2-TZVPP level).

Distance [pm]	**1 b**[a]	**3**	α-P_4S_3[b]	**2**	P_4Se_3[b]
d(M–$P_{b/coord}$)	219.8(1)	217.9(1)	–	221.3(1)	–
d(M–$P_{b/coord}$)$_{calc.}$	223.2	220.4	–	224.0	–
d($P_{b/coord}$–$P_{b/noncoord}$)	220.6(1), 221.5(1)	220.0(1), 221.7(1)	224.1	220.7(1), 221.1(1)	222.8
d($P_{b/coord}$–$P_{b/noncoord}$)$_{calc.}$	222.6	221.8, 223.3	225.5	221.8	224.6
d($P_{b/noncoord}$–$P_{b/noncoord}$)	225.7(1)	226.6(2)	–	224.9(1)	–
d($P_{b/noncoord}$–$P_{b/noncoord}$)$_{calc.}$	229.5	228.8	–	228.2	–
d($P_{b/coord}$–E)	206.6(1)	207.5(1)	210.7	221.9(1)	224.2
d($P_{b/coord}$–E)$_{calc.}$	208.4	209.3	211.0	223.7	226.2
d($P_{b/noncoord}$–E)	207.5(1), 208.1(1)	207.5(1), 208.0(2)	–	222.8(1), 223.1(1)	–
d($P_{b/noncoord}$–E)$_{calc.}$	209.8	209.9, 210.2	–	224.9	–
d(P_a–E)	210.0(1)–211.6(1)	210.1(1)–211.5(2)	210.6	224.1(1)–225.3(1)	224.9
d(P_a–E)$_{avg.}$[c]	210.7	210.6	–	224.9	–
d(P_a–E)$_{calc.}$	213.2–213.6	212.9–213.0	212.3	228.0–228.2	227.0
d(P_a–E)$_{calc./avg.}$[c]	213.4	213.0	–	228.1	–

[a] Crystals of complex **1 a** cracked in the cryostream of the diffractometer. Therefore, **1 b** was synthesized, which did not pose these problems. [b] For free P_4S_3 and P_4Se_3, d(P_b–P_b) and d(P_b–E) are given, as there are no d($P_{b/coord}$–$P_{b/noncoord}$) and d($P_{b/coord}$–E)/d($P_{b/noncoord}$–E). The average values from refs. [13] and [14] are given. [c] An average distance is only given if there are three or more different bond lengths, including the range of the distances. If there are only two different bond lengths, both bond lengths are given.

the uncoordinated cage. All $P_{b/noncoord}$–$P_{b/noncoord}$ bonds are elongated by up to 2.5 pm (in complex **3**). This is in accordance with the very small ^1J(P, P) coupling observed between these two atoms in the ^{31}P NMR spectra. The $P_{b/coord}$–E bonds and $P_{b/noncoord}$–E are also shortened by up to 4.1 pm (in complex **1 b**) in the complexes, but typically, the P_a–E bonds are less affected by coordination of the cage. However, even here, slight changes are noticeable: the P_a–E bond nearest to $P_{b/coord}$ are shortened by up to 0.6 pm in complex **1 b** and the P_a–E bonds further away from the coordinated phosphorus atom are elongated by up to 1.0 pm (in complex **1**). The Fe–$P_{b/coord}$ bond is shorter in the phosphine-substituted complex **3** than in **1 b**, which is consistent with the findings in our studies on [*Fp*–P_4]$^+$ and [*Fp*PPh_3–P_4]$^+$. It implies a stronger metal–cage bond for the more electron-rich metal fragments.[10]

Vibrational spectroscopy

The IR spectra of complexes **1 a**, **2**, and **3** show the anion bands as well as the bands of the CO ligands and several bands of the PPh_3 ligand of the cations, whereas the bands of the ligands P_4S_3 and P_4Se_3 are only visible in the Raman spectra. These spectra (Figure 4) clearly show that the coordination to the metal lowers the symmetry of the C_{3v}-symmetric cages because some degenerate bands of the ligands split upon coordination and show slightly different vibrational patterns. Generally, the experimental Raman spectra are in good agreement with the calculated spectra (see the Supporting Information, Figures S1–S3) that were used for further evaluation and band assignment.

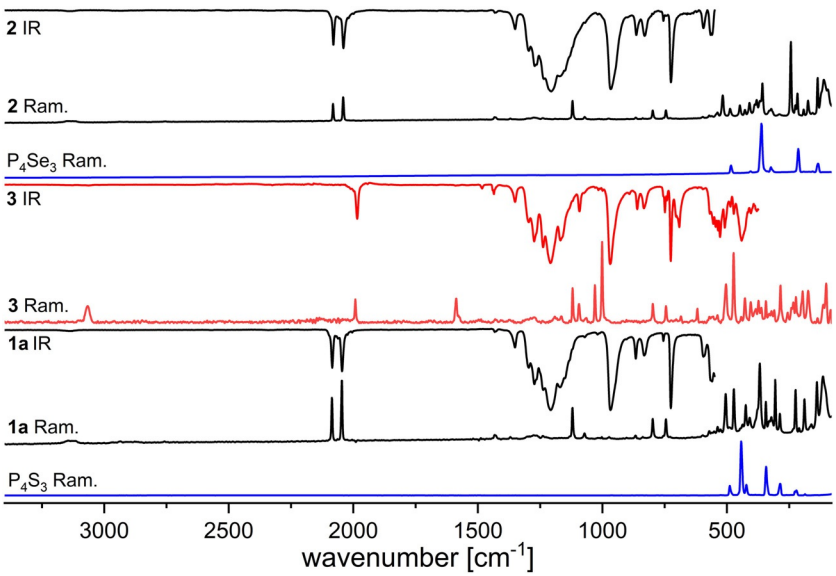

Figure 4. Vibrational spectra of complexes **1 a**, **2**, and **3** along with Raman spectra of the noncoordinated cages P_4S_3 and P_4Se_3.

Table 3. Vibrational bands of complexes **1 a**, **2**, and **3** compared to the vibrational bands of the used P_4S_3 and P_4Se_3.[a]

P_4S_3 Raman[12]	**1 a** IR	**1 a** Raman	Assignment[b]	**3** IR	**3** Raman	Assignment[b]	P_4Se_3 Raman[14][c]	**2** IR	**2** Raman	Assignment[b]
–	–	–	–	–	102 (m)	δ(Fe–CO)	–	–	–	–
–	–	115 (s)	δ(Fe–CO)	–	113 (w)	δ(Fe–CO)	–	–	111 (m)	δ(Fe–CO)
–	–	139 (s)	δ(Fe–Cp)	–	136 (vw)	δ(Fe–Cp)	135 (vw) *E*	–	136 (m)	δ(Fe–Cp)/δ(P_a–Se_3)
–	–	161 (vw)	δ(Fe–Cp)	–	174 (w)	δ(Fe–Cp)	–	–	156 (vw)	δ(OC–Fe–Cp)
–	–	189 (m)	δ(OC–Fe–Cp)	–	–	–	–	–	174 (vw)	δ(OC–Fe–Cp)
182 (vw) A_2	–	210 (vw)	δ(P_a–S_3)	–	196 (w)	δ(P_a–S_3)	214 (m) A_1/ *E*	–	192 (vw)	δ(P_b–Se)/δ(Fe–$P_{b/coord}$)
220 (vw) *E*	–	225 (s)	δ(P_b–S)	–	223 (w)	δ(P_b–S)	–	–	217 (w)	δ(P_a–Se_3)
–	–	–	–	–	241 (vw)	δ(Fe–Cp)/δ(C–H)	–	–	225 (vw)	δ(P_a–Se_3)
–	–	–	–	–	256 (vw)	δ(Fe–Cp)/δ(C–H)	–	–	244 (vs.)	δ(P_a–Se_3)
285 (w) *E*	–	288 (w)	δ(P_a–S_3)	–	285 (m)	δ(P_a–S_3)	320 (w) A_1	–	330 (vw)	δ(P_a–Se_3)/ $[Al(OR^F)_4]^-$
–	–	306 (s)	δ(P_a–S_3)	–	310 (vw)	δ(P_a–S_3)	346 (sh) *E*	-	358 (m)	$\tilde{\nu}$(P_a–Se_3)
–	–	–	–	–	321 (vw)	δ(P_a–S_3)	–	—	367 (w)	$\tilde{\nu}$(Fe–Cp)
–	–	330 (vw)	$[Al(OR^F)_4]^-$/δ(Fe–Cp)	–	330 (vw)	$\tilde{\nu}$(P_3)/$[Al(OR^F)_4]^-$	365 (vs.) A_1	–	381 (w)	δ(P_a–Se_3)
–	–	344 (m)	δ(Fe–Cp)	–	343 (w)	δ(Fe–Cp)	–	–	388 (vw)	$\tilde{\nu}$(Fe–Cp)
341 (m) *E*	–	368 (vs.)	$\tilde{\nu}$(P_3)/δ(C–H)	–	362 (vw)	$\tilde{\nu}$(P_3)/δ(C–H)	370 (sh) A_1	–	409 (vw)	$\tilde{\nu}$(P_b–Se)
–	–	377 (m)	$\tilde{\nu}$(P_3)/δ(C–H)	–	373 (w)	$\tilde{\nu}$(P_3)/δ(C–H)	405 (vw) *E*	–	428 (vw)	$\tilde{\nu}$($P_{b/noncoord}$–Se)
–	–	–	–	–	384 (vw)	δ(C–H)	–	–	448 (vw)	$\tilde{\nu}$($P_{b/coord}$–Se)/δ(Fe–C–O)
420 (vw) A_1/ *E*	–	409 (w)	$\tilde{\nu}$(P_a–S_3)	–	404 (w)	$\tilde{\nu}$(P_a–S_3)/δ(C–H)	–	–	487 (vw)	$\tilde{\nu}$(Fe–$P_{b/coord}$)/δ(Fe–C–O)
–	–	425 (m)	$\tilde{\nu}$(P_a–S_3)	-	428 (w)	$\tilde{\nu}$(P_a–S_3)/δ(C–H)	484 (w) A_1	–	517 (w)	$\tilde{\nu}$(Fe–$P_{b/coord}$)/$\tilde{\nu}$(P_3)/δ(Fe–C–O)
–	–	437 (vw)	δ(Fe–C–O)	441 (s)	443 (vw)	δ(C–H)	–	–	571 (vw)	$[Al(OR^F)_4]^-$/δ(Fe–C–O)
441 (vs.) A_1	–	472 (s)	$\tilde{\nu}$(P_b–S)	472 (w)	473 (vs.)	δ(C–H)/ $\tilde{\nu}$(P_b–S)	–	2040 (m)	2040 (w)	$\tilde{\nu}$(C–O) asy.
487 (vw) *E*	–	505 (m)	$\tilde{\nu}$(Fe–$P_{b/coord}$)/δ(P_a–Se_3)	509 (m)	504 (m)	$\tilde{\nu}$(Fe–$P_{b/coord}$)/δ(P_a–Se_3)	–	2080 (m)	2081 (w)	$\tilde{\nu}$(C–O) sy.
–	–	526 (vw)	δ(Fe–C–O)/ $\tilde{\nu}$(P_b–S)/ $[Al(OR^F)_4]^-$	528 (s)	538 (vw)	δ(C–H)/$\tilde{\nu}$(P_b–S)/δ(Fe–C–O)				
–	–	571 (vw)	$[Al(OR^F)_4]^-$/δ(Fe–C–O)	555 (m)	556 (vw)	δ(C–H)/δ(Fe–C–O)				
–	595 (w)	597 (vw)	$[Al(OR^F)_4]^-$/δ(Fe–C–O)	–	–	–				
–	2045 (m)	2046 (vs.)	$\tilde{\nu}$(C–O) asy.	–	1587 (w)	δ(C–H)				
–	2085 (m)	2086 (s)	$\tilde{\nu}$(C–O) sy.	1984 (m)	1992 (w)	$\tilde{\nu}$(C–O)				

[a] For reasons of clarity, only the cation bands are shown, and most δ(C–H) and $\tilde{\nu}$(C–H) bands are excluded. A summarizing table showing all vibrational bands is given in the Supporting Information (Table S2). All vibrational bands are given in cm^{-1}. [b] From a visualization of the calculated spectra. [c] The symmetry of the vibrational bands was derived from the calculated spectra as well as from ref. [17].

The vibrational frequencies are listed in Table 3. Vibrational bands that are directly affected by the coordination of the *Fp* and *Fp*PPh_3 moieties to the cage, such as the stretching mode $\tilde{\nu}$(P_3) (*E*), which occurs at 341 cm^{-1} for free P_4S_3, split distinctively into two bands at $\tilde{\nu}$ = 368 and 377 cm^{-1} in complex **1**. In complex **2**, this splitting was also observed at $\tilde{\nu}$ = 362 and 373 cm^{-1}. The Raman spectrum of complex **3** also shows further splittings. It is notable, that only the degenerate (*E*) bands of the free ligand show splittings in the complexes, which is due to the previously mentioned desymmetrization of the

cages upon coordination to the metal. The nondegenerate bands (A_1 and A_2) are not affected by coordination and show no further splitting.

The vibrational spectra mostly show blueshifts of the vibrational bands of the P_4S_3 and P_4Se_3 cages. Comparison reveals similar trends for both the calculated gaseous complexes as well as those observed in the solid state; that is, the distortion of the P_3 basis, the contraction of the P_b–S and P_b–Se bonds, and the shorter Fe–P_b bond in the phosphine-substituted compounds, which were also compared with the calculated gaseous free P_4S_3 and P_4Se_3 (Table 2). In addition, the calculated electron densities at the bond critical points of those structures agree with this overall bond contraction upon coordination (see below, analysis of the bonding situation with DFT methods, Table 5).

The C–O stretching frequencies indicate the poor donation capability of the cages. Thus, the stretches of the starting material *Fp*–Br (2045 and 1985 cm^{-1}) are shifted in complexes **1a** and **3** to $\tilde{\nu}$ = 2085/2045 and 2080/2040 cm^{-1}, respectively (IR and Raman). The C–O stretching frequency of the starting material *Fp*PPh_3–Br is at $\tilde{\nu}$ = 1942 cm^{-1}, and that of complex **2** is at $\tilde{\nu}$ = 1980 (IR)/1992 cm^{-1} (Raman), which corresponds to a slightly smaller blueshift, as in complexes **1a** and **3**. Similar, but more pronounced, blueshifts were also observed in [*Fp*–P_4]$^+$ and [*Fp*PPh_3–P_4]$^+$, which suggests a weaker coordination of the P_4 ligands in comparison to the P_4E_3 cages.

DFT-calculated thermodynamics of exchange reactions with other ligands

Exchange reactions of [*Fp*–P_4]$^+$ with the ligands used in this work in both the gas phase and in solution with CH_2Cl_2, as well as exchange reactions that start from either the side product [*Fp*–Br–*Fp*]$^+$ or the naked Fp^+ were calculated (Table 4). Although the synthesis of [*Fp*–As_4S_3]$^+$ and [*Fp*–As_4S_4]$^+$ salts is energetically favored, they could not be isolated; hereby, it was assumed that the ligands are dissolved in CH_2Cl_2. However, given that the solubility of the silver complexes of the nortricyclane cages decreases in the order $P_4S_3 > P_4Se_3 > A_4S_3$, with especially bad solubility for the mineral As_4S_4, it is likely that the reactions are inhibited by this issue. By contrast, this does not inhibit reaction with the comparably well-soluble silver–P_4 complex, despite being the weakest ligand.

Yet, the most favorable exchange reaction is the formation of the bridged [*Fp*–Br–*Fp*]$^+$ from residual *Fp*–Br binding the freshly formed Fp^+ cation. Thus, caution needs to be taken upon isolation of the crystalline complexes. This is reinforced by the experimentally verified isolation of the [*Fp*–Br–*Fp*]$^+$ salt (**5**). These salts tend to co-crystallize with the products, especially if the reaction mixture was not allowed to stir long enough to ensure a complete reaction. It is notable that the color of the isolated [*Fp*–*L*][WCA] salts indicates whether they are contaminated with salt **5**, as red crystals of complex **1b** contained salt **5** and pale yellow crystals of complex **1b** contained no side products. This also explains the moderate yields of the complexes, because only the good-quality crystals were isolated for further characterization. Most importantly, the calculations suggest that a ligand-transfer reaction takes place. A pre-orientated ligand is necessary for the formation of complexes **1**, **2**, and **3** to take place. Otherwise the energetically favored formation of the dimer [*Fp*–Br–*Fp*]$^+$ takes place (Scheme 2).

For *Fp*PPh_3–Br, the absence of a pre-orientated ligand is followed by CO abstraction of the residual *Fp*PPh_3–Br by the freshly generated *Fp*PPh_3^+, as shown by the reaction of *Fp*PPh_3–Br, which yields $CpFe(CO)_2PPh_3[Al(OR^F)_4]$ and was iso-

Table 4. Calculated reaction enthalpies ($\Delta_R H^0$) and free reaction energies ($\Delta_R G^0$) ((RI)B3-LYP(D3/BJ)/def2-TZVPP) of the formation of [*Fp*–L]$^+$ from [*Fp*–Br–*Fp*]$^+$ in both the gas phase and solvated in CH_2Cl_2 (two isomers, isomer 2 given in brackets.[a]

Exchange reactions of [M–Br–M]$^+$ with L to [M–P_4]$^+$ and M–Br	$\Delta_R H^\circ_{(gas)}$	$\Delta_R G^\circ_{(gas)}$	$\Delta_R G^\circ(CH_2Cl_2)$[b]
[M–Br–M]$^+$ + P_4 → [M–P_4]$^+$ + M–Br	50 [38]	45 [30]	96 [67]
[M–Br–M]$^+$ + P_4S_3 → [M–P_4S_3]$^+$ + M–Br	4 [−7]	7 [−8]	38 [10]
[M–Br–M]$^+$ + P_4Se_3 → [M–P_4Se_3]$^+$ + M–Br	−5 [−16]	−2 [−16]	23 [−5]
[M–Br–M]$^+$ + As_4S_3 → [M–As_4S_3]$^+$ + M–Br	10 [−1]	11 [−3]	21 [−8]
[M–Br–M]$^+$ + As_4S_4 → [M–As_4S_4]$^+$ + M–Br	11 [−1]	12 [−2]	19 [−10]
Exchange reactions of [M–P_4]$^+$ with L to [M–L]$^+$ and P_4	$\Delta_R H^\circ_{(gas)}$	$\Delta_R G^\circ_{(gas)}$	$\Delta_R G^\circ(CH_2Cl_2)$
[M–P_4]$^+$ + P_4S_3 → [M–P_4S_3]$^+$ + P_4	−45 (−40)	−38 (−32)	−57 (−54)
[M–P_4]$^+$ + P_4Se_3 → [M–P_4Se_3]$^+$ + P_4	−54 (−46)	−47 (−38)	−73 (−69)
[M–P_4]$^+$ + As_4S_3 → [M–As_4S_3]$^+$ + P_4	−39 (−17)	−34 (−7)	−75 (−43)
[M–P_4]$^+$ + As_4S_4 → [M–As_4S_4]$^+$ + P_4	−39 (−14)	−32 (−6)	−77 (−42)
Complexation of L by free *Fp*$^+$	$\Delta_R H^\circ_{(gas)}$	$\Delta_R G^\circ_{(gas)}$	$\Delta_R G^\circ(CH_2Cl_2)$
Fp^+ + P_4 → [*Fp*–P_4]$^+$	−160	−126	−163
Fp^+ + P_4S_3 → [*Fp*–P_4S_3]$^+$	−205	−164	−221
Fp^+ + P_4Se_3 → [*Fp*–P_4Se_3]$^+$	−214	−173	−236
Fp^+ + As_4S_3 → [*Fp*–As_4S_3]$^+$	−199	−160	−238
Fp^+ + As_4S_4 → [*Fp*–As_4S_4]$^+$	−199	−159	−240
Fp^+ + *Fp*–Br → [*Fp*–Br–*Fp*]$^+$	−210 [−198]	−171 [−157]	−259 [−230]

[a] Structures of the isomers are shown in the Supporting Information, Figures S25 and S26). Exchange reactions starting from [M–P_4]$^+$ (M$^+$ = *Fp*$^+$ and *Fp*PPh_3^+ (in parentheses) are also given. [b] The COSMO (conductor-like screening model) solvation energies were calculated at the BP86/def-TZVP level.

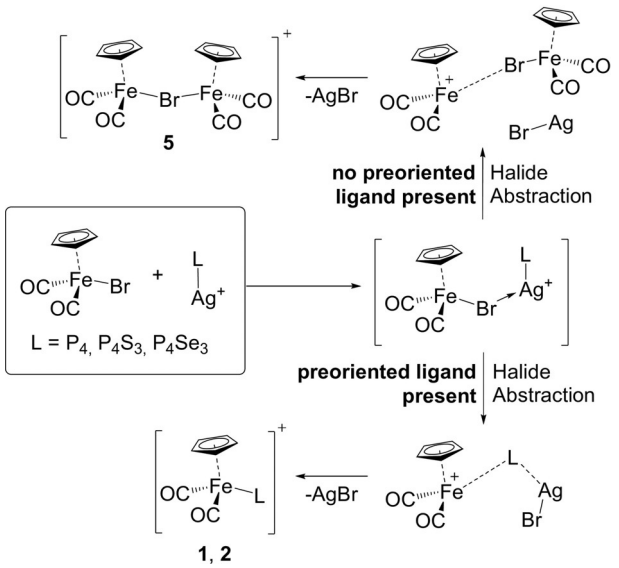

Scheme 2. Suggested ligand-transfer pathway, showing both possible scenarios with a pre-oriented ligand (bottom) and without a pre-oriented ligand (top).

lated and characterized by single-crystal XRD (scXRD) experiments after following the usual reaction procedure without the ligand.

Investigation of the bonding situation with DFT methods

The optimized gas-phase structures of the cations $[Fp{-}P_4S_3]^+$, $[Fp{-}P_4Se_3]^+$, and $[Fp\mathrm{PPh_3}{-}P_4S_3]^+$ show the same structural distortions in the cage ligands as the molecular structures of complexes **1 a**, **2**, and **3**, except for the weak distortions of the P_a–E bonds (Table 2). The structurally characterized $[Cp^*Ru(PMe_3)_2(P_4S_3)]^+$ cation, with an electron-rich metal fragment, is the only similar monomeric complex characterized by scXRD.[4] A slight structural distortion of the P_3 base and the P_b–S bonds is also present in the electron-rich complex, but it is considerably more pronounced in the complexes with the electron-poor Fp^+ and $Fp\mathrm{PPh_3}^+$ fragments. In addition, previous computational studies of the electron-rich $[Cp^*Ru(dppe)L]^+$ complexes suggested an elongation of P_a–S and P_a–Se bonds by 2–4 pm, which is not the case in the experimentally determined structures of complexes **1 b**, **2**, and **3**.[3]

The structural trends from the scXRD experiments and the calculated gas-phase structures are well reflected by the Atoms In Molecules (AIM) analysis (Table 5) of the optimized gas-phase structures of the cations in complexes **1**, **2**, and **3** and the hypothetical fragment $[Fp\mathrm{PPh_3}{-}P_4Se_3]^+$. For comparison, the data of the respective published P_4 complexes that was calculated at the same level of theory is also included. The noncoordinated P_4S_3 cage shows an electron density at the bond critical point (ρ_{BCP}) of the basal phosphorus atoms $\rho_{BCP}(P_b{-}P_b)$ of 0.709 e Å^{-3}. In $[Fp{-}P_4S_3]^+$, $\rho_{BCP}(P_{b/coord}{-}P_{b/noncoord})$ rises to 0.756 e Å^{-3}, which suggests a stronger, and thus shorter, bond between these atoms. Likewise, $\rho_{BCP}(P_{b/noncoord}{-}P_{b/noncoord})$ is lowered to 0.675 e Å^{-3}, which suggests a weaker, and thus longer, $P_{b/noncoord}$–$P_{b/noncoord}$ bond. This is also found in $[Fp{-}P_4Se_3]^+$, $[Fp\mathrm{PPh_3}{-}P_4Se_3]^+$, and the hypothetical $[Fp\mathrm{PPh_3}{-}P_4Se_3]^+$ (Table 5). The observed contractions of $d(P_{b/noncoord}{-}E)$ and $d(P_{b/coord}{-}E)$ are also reflected by an increase of ρ_{BCP} of the corresponding bonds.

The experimentally determined small distortions of the P_aE_3 apex of the cage ligands agree with similar $\rho_{BCP}(P_a{-}E)$ values of the free cages. The monophosphine-substituted analogues show slightly higher $\rho_{BCP}(Fe{-}P_{b/coord})$ and higher ellipticities of the electron density at the BCP (ε_{BCP}, Table 5) than the com-

Table 5. Calculated electron density (ρ) and ellipticity (ε) of the electron density at the BCPs of the optimized gas-phase structures ((RIJ)B3-LYP(D3-BJ)/def2-TZVPP) of P_4S_3, P_4Se_3, $[Fp{-}P_4S_3]^+$, $[Fp{-}P_4Se_3]^+$, $[Fp\mathrm{PPh_3}{-}P_4S_3]^+$, and $[Fp\mathrm{PPh_3}{-}P_4Se_3]^+$.

Property	P_4S_3	$[Fp{-}P_4S_3]^+$	$[Fp\mathrm{PPh_3}{-}P_4S_3]^+$
$\rho_{BCP}(Fe{-}P_{b/coord})$ [e Å^{-3}]	–	0.601	0.614
$\rho_{BCP}(P_{b/coord}{-}P_{b/noncoord})$ [e Å^{-3}]	0.709	0.756	0.749–0.769
$\rho_{BCP}(P_{b/noncoord}{-}P_{b/noncoord})$ [e Å^{-3}]	–	0.675	0.682
$\rho_{BCP}(P_{b/coord}{-}S)$ [e Å^{-3}]	0.864	0.925	0.904
$\rho_{BCP}(P_{b/noncoord}{-}S)$ [e Å^{-3}]	–	0.884	0.877–0.884
$\rho_{BCP}(P_a{-}S)$ [e Å^{-3}]	0.864	0.844–0.857	0.857
$\varepsilon_{BCP}(Fe{-}P_{b/coord})$	–	0.08	0.12
Property	P_4Se_3	$[Fp{-}P_4Se_3]^+$	$[Fp\mathrm{PPh_3}{-}P_4Se_3]^+$
$\rho_{BCP}(Fe{-}P_{b/coord})$ [e Å^{-3}]	–	0.594	0.607
$\rho_{BCP}(P_{b/coord}{-}P_{b/noncoord})$ [e Å^{-3}]	0.715	0.756	0.749
$\rho_{BCP}(P_{b/noncoord}{-}P_{b/noncoord})$ [e Å^{-3}]	–	0.682	0.682
$\rho_{BCP}(P_{b/coord}{-}Se)$ [e Å^{-3}]	0.736	0.783	0.769
$\rho_{BCP}(P_{b/noncoord}{-}Se)$ [e Å^{-3}]	–	0.746–0.756	0.749–0.756
$\rho_{BCP}(P_a{-}Se)$ [e Å^{-3}]	0.742	0.729	0.729–0.736
$\varepsilon_{BCP}(Fe{-}P_{b/coord})$	–	0.08	0.11
Property	P_4	$[Fp{-}P_4]^+$	$[Fp\mathrm{PPh_3}{-}P_4]^+$
$\rho_{BCP}(Fe{-}P_{b/coord})$ [e Å^{-3}]	–	0.553	0.567
$\rho_{BCP}(P_{b/coord}{-}P_{b/noncoord})$ [e Å^{-3}]	0.722	0.783–0.790	0.783–0.803
$\rho_{BCP}(P_{b/noncoord}{-}P_{b/noncoord})$ [e Å^{-3}]	–	0.682–0.688	0.682–0.702
$\varepsilon_{BCP}(Fe{-}P_{b/coord})$	–	0.09	0.14

plexes of the more electron-poor Fp^+. This suggests a stronger Fe–$P_{b/coord}$ bond in the more electron-rich complexes, which is in agreement with an increased π back-bonding of the more electron-rich metal fragments. This is also supported by the variety of complexes that are accessible with electron-rich bisphosphine and/or Cp*-substituted metal fragments.

Generally, ρ_{BCP}(Fe–$P_{b/coord}$) is higher in complexes **1**, **2**, and **3** than in the previously reported cations $[Fp–P_4]^+$ and $[FpPPh_3–P_4]^+$, which shows that P_4S_3 and P_4Se_3 are more strongly bound than P_4; this is also reflected by the calculated exchange reactions that show the P_4 complexes to be the least favorable (Table 4). The ρ_{BCP} are also reflected in the vibrational spectra by showing significant blueshifts of some vibrational modes of the cages owing to the cage contractions. As in our investigations on cations $[Fp–P_4]^+$ and $[FpPPh_3–P_4]^+$, computed partial charges as well as Wiberg bond orders have shown no definite trends and partially profound disagreements[10] (see the Supporting Information, Table S4); therefore, they were not used for further discussion.

MO considerations

To understand the nature of the cage contractions, we turned to MO investigations. Figure 5 indicates that the interaction of the orbitals of the free P_4E_3 cages with those of the iron fragments in Fp^+ show a modified bonding situation to $[Fp–P_4]^+$. In the latter, the cage contraction was assigned to the removal of electron density from the slightly P–P antibonding P_4-HOMO by π donation into the LUMO+1 of the Fp^+ fragment.[10] In contrast to P_4, the HOMO of the P_4E_3 cages allows for σ and π donation towards the LUMO (σ)/LUMO+1 (π) of the metal fragment. Still, the P_4E_3 cage HOMO has antibonding character along the P_b–E bonds and two of the three P–P bonds. Therefore, the removal of electron density from these orbitals presumably induces the observed cage contraction. In addition, the third P–P bond (back side $P_{b/noncoord}$–$P_{b/noncoord}$) is P–P bonding in the cage HOMO. Thus, this bond is weakened through the interaction in the molecular structure.

This higher σ character of the Fe–$P_{b/coord}$ bonds in $[Fp–P_4E_3]^+$ compared to $[Fp–P_4E_3]^+$ goes along with the calculated slight decrease of ε_{BCP}(Fe–$P_{b/coord}$) and is the reason for the higher ρ_{BCP}(Fe–$P_{b/coord}$) in complexes **1**, **2**, and **3** than the P_4 analogues (Table 5). This stronger Fe–$P_{b/coord}$ bond in complexes **1**, **2**, and **3** manifests itself in the calculated higher thermodynamic stability of these complexes as well as in the static nature of the ^{31}P NMR signals, compared with the temperature-dependent fluxional nature of $[Fp–P_4]^+$ and $[FpPPh_3–P_4]^+$.

Conclusions

Investigations towards ligand-transfer reactions of silver complexes with the inorganic cages, such as the almost insoluble nortricyclane cage As_4S_3 and the realgar cage As_4S_4, were futile and led to salts of the already known cations $[Fp–Br–Fp]^+$ and

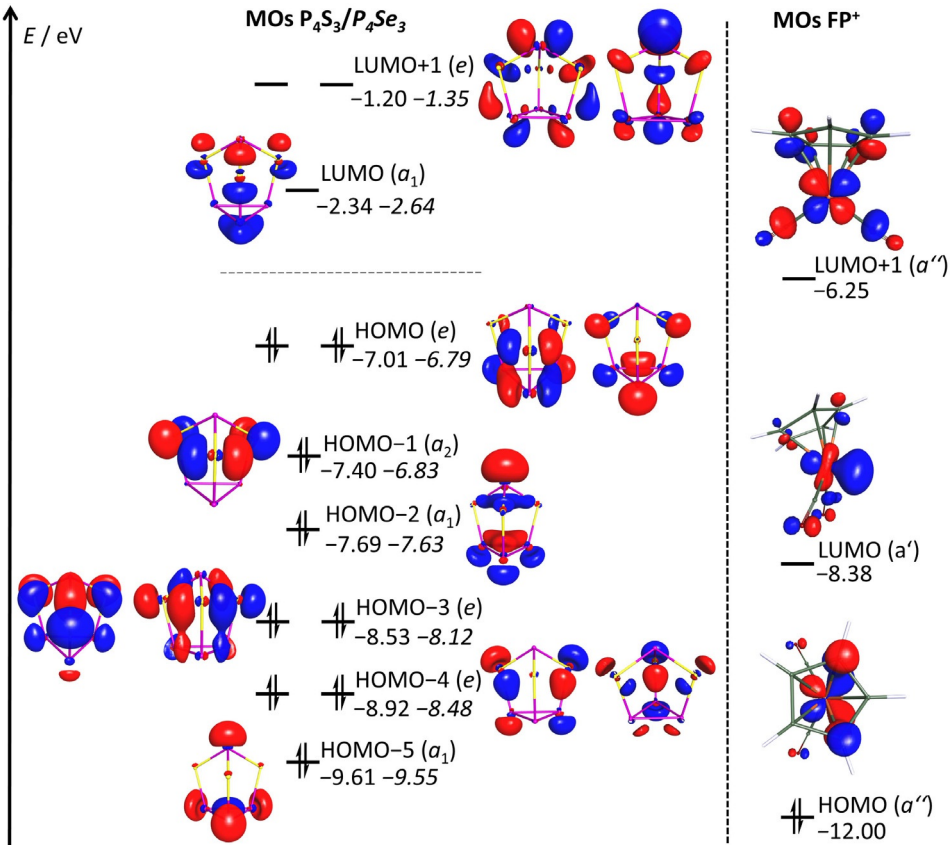

Figure 5. Molecular orbitals of the P_4E_3 cages (left: P_4S_3 in standard letters, P_4Se_3 in italics) and frontier orbitals of Fp^+ (right) calculated at (RIJ)B3-LYP/D3(BJ)/def2-TZVPP.

$[Au(PPh_3)_2]^+$. By contrast, the reactions with the more soluble silver complexes of the phosphorus-containing cages P_4S_3 and P_4Se_3 gave stable salts of the hitherto unknown cations $[Fp{-}P_4S_3]^+$, $[Fp{-}P_4Se_3]^+$, and $[FpPPh_3{-}P_4S_3]^+$. NMR experiments showed that, contrary to the highly fluxional binding of the P_4 complexes at the metal fragments, no dynamic chemical exchange processes occur between the phosphorus atoms of these clusters, even at room temperature in solution. Hence, the title complexes form static adducts through one firmly bound basal phosphorus atom. This is supported by their solid-state structures that show η^1-P_b coordination. Cage contractions, similar to the P_4 analogues, manifested themselves in the molecular structures as well as in the optimized gas-phase DFT structures and in AIM analyses. The vibrational spectra reflect these observations and show characteristic splittings and blueshifts of the Raman bands of the ligands. Also, the coupling constants observed in the NMR spectra indicate these special binding situations. MO investigations revealed similar reasons for the contraction as in complex $[Fp{-}P_4]^+$. However, the herein presented complexes exhibit additional σ donations from the ligand to the metal fragment. In general terms, the prevention of π back-donation by using electron-poor metal fragments may lead to bond contractions, given that the donating cage orbitals include some antibonding character. In this respect, there is some analogy to the "non-classical" or "σ-only bound" transition-metal/CO complexes.[18]

Acknowledgements

This work was supported by the Albert–Ludwigs-Universität Freiburg and by the DFG in the *Normalverfahren*. We would like to thank Fadime Bitgül for the measurement of the NMR spectra and Dr. Daniel Himmel for valuable discussions the DFT calculations.

Conflict of interest

The authors declare no conflict of interest.

Keywords: cage compounds · iron · main group elements · transition metals · weakly coordinating anion

[1] a) M. Di Vaira, M. Peruzzini, P. Stoppioni, *Inorg. Chem.* **1983**, *22*, 2196; b) M. Di Vaira, M. Peruzzini, P. Stoppioni, *J. Organomet. Chem.* **1983**, *258*, 373; c) M. Herberhold, G. Frohmader, J. Peukert, W. Milius, *Z. Naturforsch. B* **2000**, *55*, 1188; d) G. Balázs, A. Biegerl, C. Gröger, J. Wachter, R. Weihrich, M. Zabel, *Eur. J. Inorg. Chem.* **2010**, 1231; e) C. Aubauer, E. Irran, T. M. Klapötke, W. Schnick, A. Schulz, J. Senker, *Inorg. Chem.* **2001**, *40*, 4956; f) A. W. Cordes, R. D. Joyner, R. D. Shores, E. D. Dill, *Inorg. Chem.* **1974**, *13*, 132; g) A. Biegerl, D. Piryazev, M. Scheer, J. Wachter, A. Virovets, M. Zabel, *Eur. J. Inorg. Chem.* **2011**, 4248.

[2] a) E. Guidoboni, I. de los Rios, A. Ienco, L. Marvelli, C. Mealli, A. Romerosa, R. Rossi, M. Peruzzini, *Inorg. Chem.* **2002**, *41*, 659; b) M. Di Vaira, M. Peruzzini, S. S. Costantini, P. Stoppioni, *J. Organomet. Chem.* **2010**, *695*, 816; c) M. Di Vaira, I. de los Rios, F. Mani, M. Peruzzini, P. Stoppioni, *Inorg. Chem. Commun.* **2002**, *5*, 879.

[3] M. Di Vaira, I. de los Rios, F. Mani, M. Peruzzini, P. Stoppioni, *Eur. J. Inorg. Chem.* **2004**, 293.

[4] M. Caporali, F. D. Calvo, C. Bazzicalupi, S. Seniori Costantini, M. Peruzzini, *J. Organomet. Chem.* **2018**, *859*, 68.

[5] P. Barbaro, M. Di Vaira, M. Peruzzini, S. Seniori Costantini, P. Stoppioni, *Chem. Eur. J.* **2007**, *13*, 6682.

[6] a) B. M. Cossairt, C. C. Cummins, *J. Am. Chem. Soc.* **2009**, *131*, 15501; b) I. de los Rios, J.-R. Hamon, P. Hamon, C. Lapinte, L. Toupet, A. Romerosa, M. Peruzzini, *Angew. Chem. Int. Ed.* **2001**, *40*, 3910; *Angew. Chem.* **2001**, *113*, 4028.

[7] C. Schwarzmaier, A. Y. Timoshkin, M. Scheer, *Angew. Chem. Int. Ed.* **2013**, *52*, 7600; *Angew. Chem.* **2013**, *125*, 7751.

[8] C. Schwarzmaier, M. Sierka, M. Scheer, *Angew. Chem. Int. Ed.* **2013**, *52*, 858; *Angew. Chem.* **2013**, *125*, 891.

[9] a) P. E. Riley, R. E. Davis, *Organometallics* **1983**, *2*, 286; b) T. S. Janik, L. M. Krajkowski, M. R. Churchill, *J. Chem. Crystallogr.* **1995**, *25*, 751; c) J. Zheng, L. C. Misal Castro, T. Roisnel, C. Darcel, J.-B. Sortais, *Inorg. Chim. Acta* **2012**, *380*, 301; d) A. G. M. Barrett, N. E. Carpenter, M. Sabat, *J. Organomet. Chem.* **1988**, *352*, C8–C12.

[10] I. M. Riddlestone, P. Weis, A. Martens, M. Schorpp, H. Scherer, I. Krossing, *Chem. Eur. J.* **2019**, *25*, 10546–10551.

[11] a) T. S. Cameron, A. Decken, I. Dionne, M. Fang, I. Krossing, J. Passmore, *Chem. Eur. J.* **2002**, *8*, 3386; b) D. Aris, J. Beck, A. Decken, I. Dionne, J. Schmedt auf der Günne, W. Hoffbauer, T. Köchner, I. Krossing, J. Passmore, E. Rivard, F. Steden, X. Wang, *Dalton Trans.* **2011**, *40*, 5865; c) T. Köchner, N. Trapp, T. A. Engesser, A. J. Lehner, C. Röhr, S. Riedel, C. Knapp, H. Scherer, I. Krossing, *Angew. Chem. Int. Ed.* **2011**, *50*, 11253; *Angew. Chem.* **2011**, *123*, 11449; d) I. Krossing, L. van Wüllen, *Chem. Eur. J.* **2002**, *8*, 700; e) P. Weis, D. Kratzert, I. Krossing, *Eur. J. Inorg. Chem.* **2018**, 3203.

[12] A. Adolf, M. Gonsior, I. Krossing, *J. Am. Chem. Soc.* **2002**, *124*, 7111.

[13] I. Raabe, S. Antonijevic, I. Krossing, *Chem. Eur. J.* **2007**, *13*, 7510.

[14] P. Weis, C. Hettich, D. Kratzert, I. Krossing, *Eur. J. Inorg. Chem.* **2019**, 1657.

[15] a) R. Schneider, I.-P. Lorenz, H. Nöth, W. Ponikwar, *Z. Anorg. Allg. Chem.* **2001**, *627*, 1775; b) R. J. Staples, C. King, M. N. I. Khan, R. E. P. Winpenny, J. P. Fackler, Jr., *Acta Crystallogr. Sect. C* **1993**, *49*, 472.

[16] Compound **1b** crystallized in the triclinic space group $P\bar{1}$ (No.: 2) with $a=13.0589(5)$ Å, $b=14.1991(6)$ Å, $c=16.6335(7)$ Å, $\alpha=85.512(2)^\circ$, $\beta=70.409(2)^\circ$, $\gamma=79.648(2)^\circ$, and $Z=2$. The anions show disorder; however, there is no disorder in the cation. Compound **2** also crystallized in the triclinic space group $P\bar{1}$ (No.: 2) with the cell parameters $a=11.7416(5)$ Å, $b=12.0319(5)$ Å, $c=16.1237(7)$ Å, $\alpha=86.314(2)^\circ$, $\beta=75.701(2)^\circ$, $\gamma=79.648(2)^\circ$, and $Z=2$. The anion is heavily disordered; however, there is no disorder in the cation. Compound **3** crystallizes in the monoclinic space group $P2_1/c$ (No.: 14) with $a=19.097(2)$ Å, $b=17.883(2)$ Å, $c=18.694(2)$ Å, $\beta=117.453(4)^\circ$, and $Z=4$. The crystal structure of this compound had to be determined at 170 K. Upon further cooling, a splitting of the reflexes, which indicated formation of a superstructure, was observed. Again, the anion is heavily disordered, but not the cation.

[17] W. Bues, M. Somer, W. Brockner, *Z. Naturforsch. B* **1980**, *35*, 1063.

[18] a) H. Willner, F. Aubke, *Angew. Chem. Int. Ed. Engl.* **1997**, *36*, 2402; *Angew. Chem.* **1997**, *109*, 2506; b) H. Willner, F. Aubke, *Chem. Eur. J.* **2003**, *9*, 1668; c) Q. Xu, *Coord. Chem. Rev.* **2002**, *231*, 83.

[19] CCDC 1890335, 1890336, 1890337, 1890339, and 1890338, 1901739 **1b**, **2**, **3**, **4**, **5**, and (CpFe(CO)2PPh3[Al(ORF)4]), respectively, contain the supplementary crystallographic data for this paper. These data are provided free of charge by The Cambridge Crystallographic Data Centre.

Manuscript received: May 22, 2019
Revised manuscript received: July 9, 2019
Accepted manuscript online: July 9, 2019
Version of record online: August 23, 2019

